

EXPERIMENTAL AND NUMERICAL INVESTIGATION OF A STRUCTURAL-DYNAMICALLY SCALED DELTA WING WITH TRAILING EDGE FLAPS

Konstantin Bantscheff¹, Francesco Santelli¹ & Christian Breitsamter¹

¹Technische Universität München, Chair of Aerodynamics and Fluid Mechanics, Boltzmannstraße 15, Garching, Germany

Abstract

This work focuses on an experimental investigations of a delta wing fuselage configuration in the low-speed wind tunnel W/T-A facility of the Chair of Aerodynamics and Fluid Mechanics at the Technical University of Munich. The influence of different trailing edge flap deflections on the aerodynamic characteristics is studied. For the aerodynamic analyses, force and moment measurements, Particle Image Velocimetry (PIV) measurements and a Fast Response Aerodynamic Probe (FRAP) measurement are conducted. A power spectral density analysis of velocity and pressure fluctuations is used to detect dominant frequencies of the two emerging vortex systems above the wing and compared to an analytical prediction method. Additionally, the wing is designed to be aeroelastically scaled. Thus, the deformation of the model is also investigated applying a photogrammetry measurement setup. At last, a comparison with aeroelastic simulations is conducted.

Keywords: Aeroelasticity, Fast Response Aerodynamic Probe, Delta wing

1. Introduction

The exploration of highly agile delta-wing configurations incorporating deformable structures holds major significance within aeronautical research for many reasons. First, the examination of static structural deformations and stresses arising from applied aerodynamic loading stands pivotal in the aircraft design process. Secondly, the intricate interplay between the aerodynamics and the structure of an aircraft, commonly known as fluid-structure interaction (FSI), generates structural dynamic phenomena. Moreover, the consideration of structural dynamics retroactively influences the aerodynamics of the aircraft, a phenomenon imperceptible in rigid layouts.

In order to understand the loads acting on the wing, a general knowledge regarding the occurring aerodynamics for delta wings at moderate speeds and and high angles of attack is essential. These conditions trigger complex fluid dynamics, which have been subject to numerous investigations over decades of research [1, 2]. The airflow on highly swept wings with low to medium aspect ratios manifests in the emergence of vortex systems and regions characterized by intense separated flow, particularly noticeable at medium to high angles of attack.

Modifying classical delta wing structures leads to the emergence of more complex vortex patterns, in particular, when multiple vortex systems are interacting. In that regard, multiple studies have been conducted to investigate the flow characteristics for double ([3]) and triple ([4]) delta wing configurations. Furthermore, to manipulate vortex systems, leading and trailing edge high lift devices can be applied ([5, 6]).

A stable vortex system is characterized by high axial velocities in the core of the vortex. However, the vortex structure undergoes structural changes as the angle of attack increases above a certain level. The stability of the structure can not be maintained and vortex bursting occurs due to an adverse pressure gradient along the vortex axis. This phenomenon increases the vortex diameter and induces turbulence in the core as well as reduced axial velocities in the core. Furthermore, dominant quasi periodic fluctuations are developed, which are referred to as vortex induced buffet.

Consequently, the aerodynamic surfaces of the aircraft structure endure pressure fluctuations with the resultant structural response termed buffeting [7]. The impact of the vortex structures and in general the aerodynamic forces on the aircraft's structure is of major importance for the design process and has thus be investigated experimentally as well. Therefore, the structural modeling of the wing's internal components plays a vital role. Different design methods can be chosen for the structural design. Stenfelt et al. [8] investigated an aeroelastic design of an assembled delta wing model with integrated control surfaces, tuning overall wing stiffness by using a combination of multiple materials. Alternatively, Gibson et al. [9] used an integral design approach to mill a wing structure out of an aluminum block, accepting the time and resource intensive manufacturing procedure. Latest advancements in additive manufacturing also enabled the design of complex and large structures in a monolithic layout, which has been applied by Khan and Tsushima[10, 11]. Apart from the experimental analysis, the generation of an adequate clone of the wing model for numerical investigations is a challenging task. However, advancements in computational capabilities have paved the way for sophisticated methods to perform fluid-structure interactions numerically as well, facilitating data exchange between structural meshes and aerodynamic grids [12, 13]. A coupled aeroelastic simulation of a generic low sweep delta wing has been conducted by Attar et. al. [14] or for a more complex aircraft configuration by Katzenmeier et. al. [15].

The major aim of performing both experimental and numerical data is to validate the computational predictions by the experimental data sets. In that regard, this paper uses an aeroelastic scaling approach for a delta wing configuration with a fuselage based on previous work [16] to design a 3D printed wind tunnel model in order to perform experimental analyses. Moreover, the delta wing at hand features a deployed slat and adjustable trailing edge flaps to manipulate the vortex structure in particular in the high angle of attack range. Experimental force and moment investigations are conducted as well as optical flow visualization methods and probe measurements. The elastic deformation of the wind tunnel model is captured by a stereo photogrammetry method. The gathered data is used to verify the simulation results of a two-way coupled simulation of the delta wing model.

2. Model Description

2.1 Aerodynamic Design

Here, a half model of a highly agile aircraft, called *Model53c* is considered scaled by a factor of 11.2 with respect to a fictive full scale configuration. The configuration consists of a generic fuselage, a delta wing and two trailing edge flaps. Furthermore, the wing includes a leading edge slat, which is deployed at an angle of $\delta_S = 20^\circ$. The delta wing exhibits a leading edge sweep angle of $\phi = 53^\circ$ and an aspect ratio of $\Lambda = 2.11$, while the taper ratio is $\lambda_t = 0.159$. Additionally, a continuous wing twist distribution is applied and results in a twist angle of -1.50° at the wing tip. Figure 1 shows the geometric parameters of the configuration as well as a body fixed frame of reference at the apex of the wing. The according dimensional data is given in Table 1.

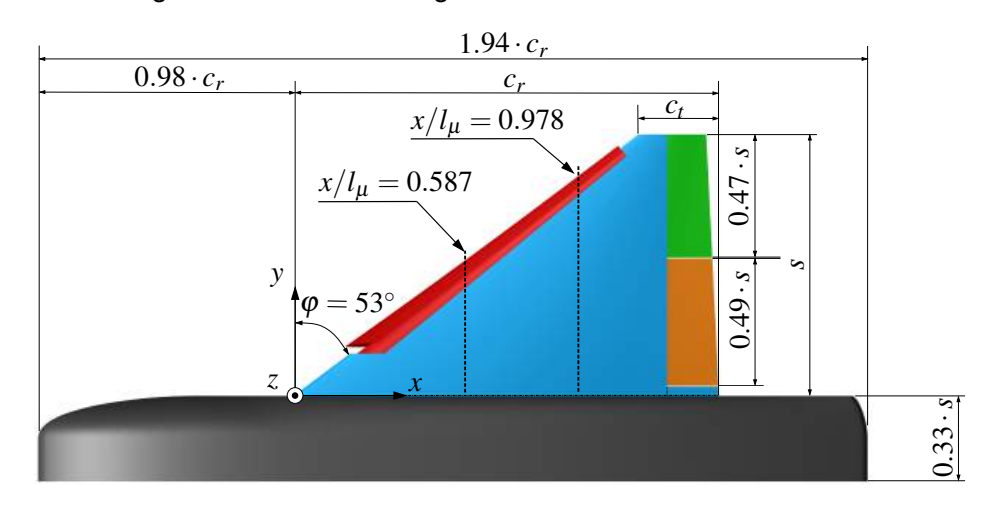


Figure 1 – Geometric parameters of the *Model53c*

Quantity	Value
Half span	$s = 0.458 \mathrm{m}$
Root chord	$c_r = 0.750 \mathrm{m}$
Tip chord	$c_t = 0.120 \mathrm{mm}$
Mean aerodynamic chord	$l_{\mu} = 0.511 \mathrm{m}$
Wing reference area	$S_{ref} = 0.398 \mathrm{m}^2$
Aspect ratio	$\Lambda = 2.11$
Taper ratio	$\lambda_t = 0.159$
Sweep	$\varphi = 53^{\circ}$
Slat angle	$\delta_S = 20^\circ$

Table 1 – Geometric data of the wind tunnel model

t_{rib}	t_{spar}	$t_{spar,TE}$	$t_{s,r}$	$t_{s,t}$
(m)	(m)	(m)	(m)	(m)
0.0023	0.0045	0.0090	0.0020	0.0011

Table 2 – Thickness data of the internal structure

2.2 Structural Model

As the wing and flaps are considered to be flexible, the inner structure is taken into account for the analysis as well. Therefore, the structure of the wing is optimized, factoring in the characteristics of a suitable material. To ensure the fabrication of a pseudo-monolithic part provided with a high level of microstructural isotropy, stereolithographic (SLA) printing using polypropylene is applied [17]. The Accura Xtreme series is selected as the basis for the wing's and flaps' structural layout, exhibiting a density of $\rho=1180\,\mathrm{kg\,m^{-3}}$ in its cured state [18] and a global Young's modulus of $E=1.768\,\mathrm{GPa}$, which is identified using a deformation test rig.

The structural layout of the wing consists of a rib, spar, and skin design, with component thicknesses optimized based on insights from previous studies (see [16]). The wing's structure comprises five ribs, including a tip rib and a root section, along with twelve spars and a trailing edge spar, all enveloped by the skin. Each rib maintains an identical thickness, denoted as t_{rib} , while the spars, except for the trailing edge spar ($t_{spar,TE}$), share a uniform thickness, designated as t_{spar} . The skin thickness remains consistent between two ribs, gradually decreasing towards the wing tip in distinct increments. Hence, the skin thickness distribution is defined by the thickness at the root ($t_{s,r}$) and at the tip ($t_{s,t}$), as detailed in Table 2. As for the control surfaces, they are divided into outer and inner flaps, both designed as solid material.

2.3 Wind Tunnel Model Application

The wing is attached to a metal mount, which is connected to the force and moment sensor. The inner and outer flap are bolted to the trailing edge section of the wing and can be exchanged for flaps with different deflection angles. Flap angles from -30° to 30° are available in 10° -steps. The fuselage has a shielding role and covers the mount. Furthermore, it is mechanically disconnected from the force and moment sensor and thus from the wing. A foam sealing is used to reduces leakage effects between the fuselage and the wing.

3. Wind Tunnel Experiments

All measurements are conducted within the wind tunnel facility A of the Chair of Aerodynamics and Fluid Mechanics at the Technical University of Munich, utilizing a Göttingen-type wind tunnel. The measurement area exhibits dimensions of $2.4\,\mathrm{m}$ in width, $1.8\,\mathrm{m}$ in height and $4.8\,\mathrm{m}$ in length. For the open test section the wind tunnel maintains a maximum turbulence intensity of $0.4\,\%$. Two different dynamic pressures are examined in the wind tunnel. The resulting conditions are listed in Table 3.

Parameter	Value		
	Condition 1	Condition 2	
Mach number Ma	0.090	0.144	
Dynamic pressure q	532 Pa	1476Pa	
q/E ratio	0.3×10^{-6}	0.8×10^{-6}	

Table 3 – Investigated flow conditions

3.1 Force and Moment Measurements

Global forces and moments are captured by an external six-component force sensor situated beneath the wind tunnel's test section. The sensor is capable of withstanding maximum sustainable loads of $\pm 1500\,\mathrm{N},\ \pm 3000\,\mathrm{N},\$ and $\pm 3000\,\mathrm{N}$ for axial, lateral, and normal forces, respectively. Additionally, it can endure maximum sustainable moments of $\pm 700\,\mathrm{N},\ \pm 500\,\mathrm{N},\$ and $\pm 700\,\mathrm{N}$ for rolling, pitching, and yawing moments, correspondingly. Moreover, the sensor has a measurement accuracy of $0.025\,\%$ concerning the total load range of the balance.

The accuracy of the aerodynamic coefficients for the investigated model is detailed in Table 4, show-casing their repeatability. Here, the repeatability is defined as the standard deviation of coefficients derived from 6 measurement repetitions. The standard deviation, as depicted in the table, is determined for undeflected flaps, with a q/E-ratio of $q/E = 0.3 \times 10^{-6}$, for multiple angles of attack.

Coefficient	Standard deviation at multiple AoA		
	20°	25°	30°
C_L	0.006	0.004	0.004
C_D	0.001	0.002	0.002
C_m	0.004	0.004	0.004

Table 4 – Repeatability of measured force and moment coefficients for $\delta=0^\circ$ and $q/E=0.3\times 10^{-6}$

3.2 PIV Measurements

Employing a Stereo-Particle Image Velocimetry measurement setup, the flow characteristics above the upper wing surface are investigated across various cross-flow sections. To enable a precise and efficient measurement of multiple planes over the entire wing, the Stereo-PIV system is mounted above the wind tunnel test section at a traversal system (see Figure 2). That way, the alignment of the laser sheet with respect to the surface of the wing and the calibration of the cameras needs to be conducted for each investigated angle of attack. Positioned upstream and downstream of the measurement plane are two sCMOS cameras with a resolution of 2560×2160 pixels. Seeding particles, with less than $1\,\mu\mathrm{m}$ in diameter, were introduced into the test section to enable the visualization of the flow characteristics. Figure 2 also depicts the resulting PIV laser sheet, creating a cross-flow plane. The cameras, which are operating at a sampling frequency of $f=15\,\mathrm{Hz}$, take 400 sets of image pairs for each investigated cross-section. The findings presented in this study are derived from the mean and root mean square values extracted from analyzing these 400 samples. The associated uncertainties of the three mean velocity components were quantified as u_{err}/U_{∞} , v_{err}/U_{∞} , $w_{err}/U_{\infty} < 0.05$ [19].

3.3 FRAP Measurements

In order to ascertain time resolved quantities of the 3-dimensional velocity field across the delta wing configuration, an intrusive measurement is carried out utilizing a fast response aerodynamic probe (FRAP), illustrated in Figure 3.

The hemispherical probe head features five ports which are connected to piezo-resistive pressure sensors (Meggitt Endevco 8507C-2). During the measurements the ambient pressure outside the wind tunnel test section serves as the reference pressure for the differential sensors. The probe is

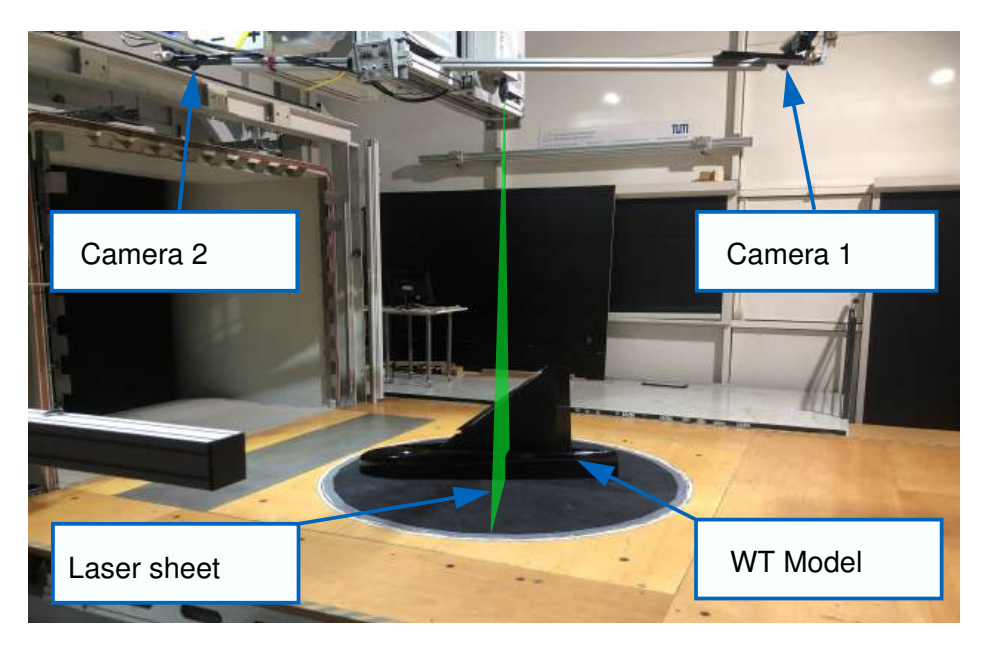


Figure 2 – PIV setup for the Model53c

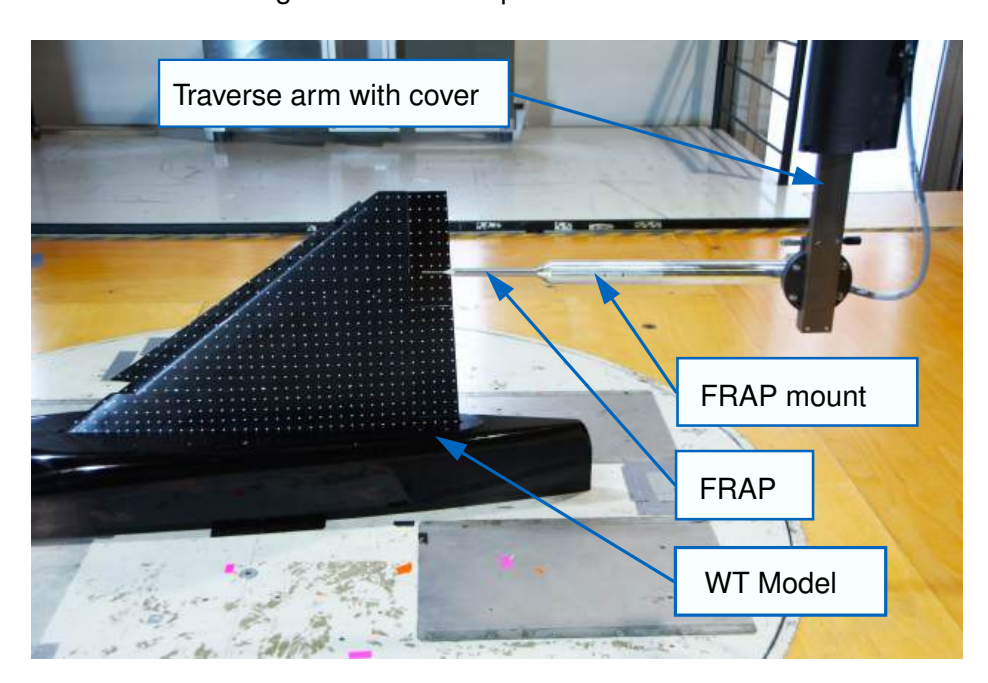


Figure 3 – FRAP setup for the *Model53c*

linked to two NI 9237 data acquisition cards, which relay the data to a measurement computer. Prior to the measurements, the probe undergoes a spatial calibration process, covering various velocity and angle combinations. As a result, the velocity reconstruction is feasible in a spatial range up to $\pm 60^{\circ}$. Reconstructed flow vectors outside the calibration cone (e.g. reversed flow regions or high flow angles) are excluded of the corresponding data set. Moreover, a temporal calibration of the cavity system within the probe has been conducted to account for the acoustic resonance and attenuation effects of the pressure ports on the unsteady flow measurements. Subsequently, for the flow field reconstruction, the obtained pressures are post-processed with calibration data from both temporal and spatial calibrations. This process yields reconstruction accuracies below 0.2° in flow angles and $0.1\,\mathrm{m\,s^{-1}}$ in reconstructed velocity. A maximum sampling rate of $10\,\mathrm{kHz}$ is achievable [20]. To mitigate aliasing effects, a low-pass filter below the Nyquist frequency at $f = 0.45 \cdot f_s$ is implemented in the NI measurement cards. The measurement duration is set to $t_s = 10\,\mathrm{s}$.

3.4 Photogammetry Setup

The occurring deformation of the elastic *Model53c* is determined by a stereo photogrammetry measurement. Figure 4 depicts the utilized setup in the wind tunnel test section.

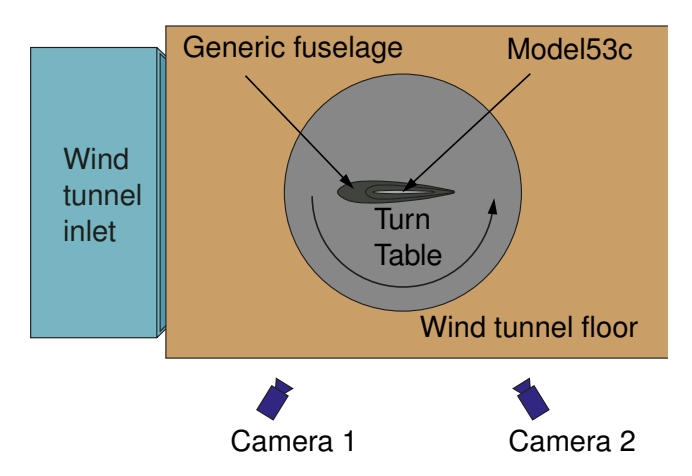


Figure 4 – Illustration of the stereo photogrammetry setup

Two CMOS cameras with a distance of $2.4\,\mathrm{m}$ between each other are used to acquire photos of the upper side of the delta wing configuration. The cameras exhibit a maximum frame rate of $14\,\mathrm{Hz}$ and a resolution of 2592×1944 pixels, which corresponds to a spatial resolution of $0.33\,\mathrm{mm}$ per pixel. For this series of experiments, the recording is conducted at an aperture of f/8 and an exposure time of $80\,\mathrm{ms}$. For the calibration of the cameras, a flat plate with a 7×8 checkerboard pattern. Multiple sets of pictures in various positions and orientations of the calibration target are captured to perform the stereo camera calibration. The MATBLAB's Stereo Camera Calibrator app is then employed to estimate the intrinsic and extrinsic parameters of the two camera setup. The mean reprojection error of the calibration procedure amounts to 0.08 pixels. To enable the identification of the deformed upper wing shape, over 500 white markers with a diameter of $3\,\mathrm{mm}$ are placed on the upper side of the wing and the flaps in a Cartesian pattern each $2\,\mathrm{cm}$ distant from each other. In the post processing step, the centers of those markers are identified and matched between the two stereo pictures. Afterwards MATLAB's Stereo Vision toolbox is utilized to reconstruct the 3D coordinates of all recognised points by applying a triangulation function taking into account the calibration data of the cameras [21]. The precision of the photogrammetry setup is assessed by comparing the reconstructions of the

upper surface of the wing from three image pairs. The pictures are captured consecutively with the wind tunnel turned off, while the angle of attack and the flap angle are respectively set to $\alpha=20^\circ$ and $\delta=0^\circ$. Table 5 summarizes the maximum root mean square error (*RMSE*) values of the measurement points. The *RMSE* value are computed based on the deviation of the measurement point location in the *X*, *Y* and *Z* directions. A minor directional dependency is noted, with *X* and *Y* directions yielding maximum *RMSE* values below $50\,\mu\text{m}$ and the *Z* direction below $130\,\mu\text{m}$. Overall the *RMSE* values indicate adequate precision considering the investigated wing deformation.

Quantity	Value [mm]
Maximum <i>RMSE</i> in <i>X</i> direction	0.0436
Maximum RMSE in Y direction	0.0464
Maximum <i>RMSE</i> in <i>Z</i> direction	0.1224

Table 5 – Repeatability of the stereo photogrammetry measurement setup.

Figure 5 depicts the *RMSE* distribution regarding the total displacement $RMSE_{Tot}$ of the reconstructed point cloud. The plot doesn't show any relevant dependency on the position of the collocation point in the distribution. Furthermore, all values fall below $130\,\mu\text{m}$, with most clustering around the mean value of $40\,\mu\text{m}$. The histogram shows a Gaussian distribution of the collocation point count with a peak at $30\,\mu\text{m}$. More than 90% of the data points lie below $75\,\mu\text{m}$ of accuracy, indicating a positive skewness towards lower values.

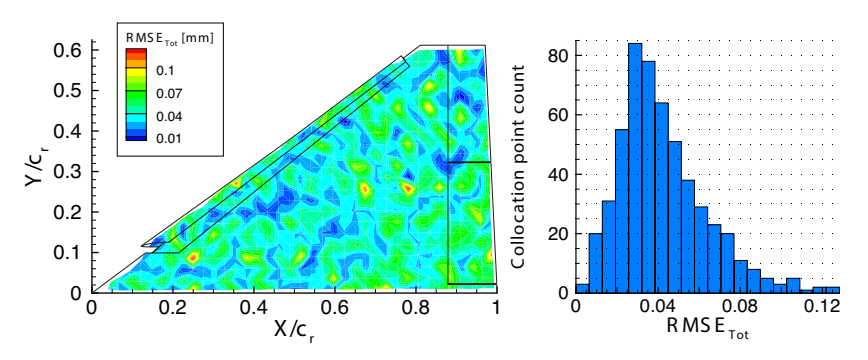


Figure 5 – Plot of the total RMSE distribution $RMSE_{Tot}$ on the upper surface of the wing and histogram displaying the collocation point count over the total RMSE values.

4. Numerical Setup

This section focuses on the numerical analysis of the *Model53c*. Dynamic aeroelastic loads acting on the wind tunnel model are simulated through a strong two-way fluid-structure coupling method, integrating Computational Fluid Dynamics (CFD) analysis with a structural Finite Element Method (FEM) model.

4.1 Computational Fluid Dynamics

At first, the fluid dynamics side of the coupling procedure is explained. Transient Computational Fluid Dynamics (CFD) simulations are conducted using Ansys Fluent, employing the unsteady Reynolds-averaged Navier-Stokes (U-RANS) equations. The SST k- ω turbulence model closes the compressible, three-dimensional RANS equations. A pressure-based solution method utilizes a SIMPLE pressure-velocity coupling, enforcing mass conservation and determining the pressure field [22]. The spatial discretization employs a second-order upwind scheme.

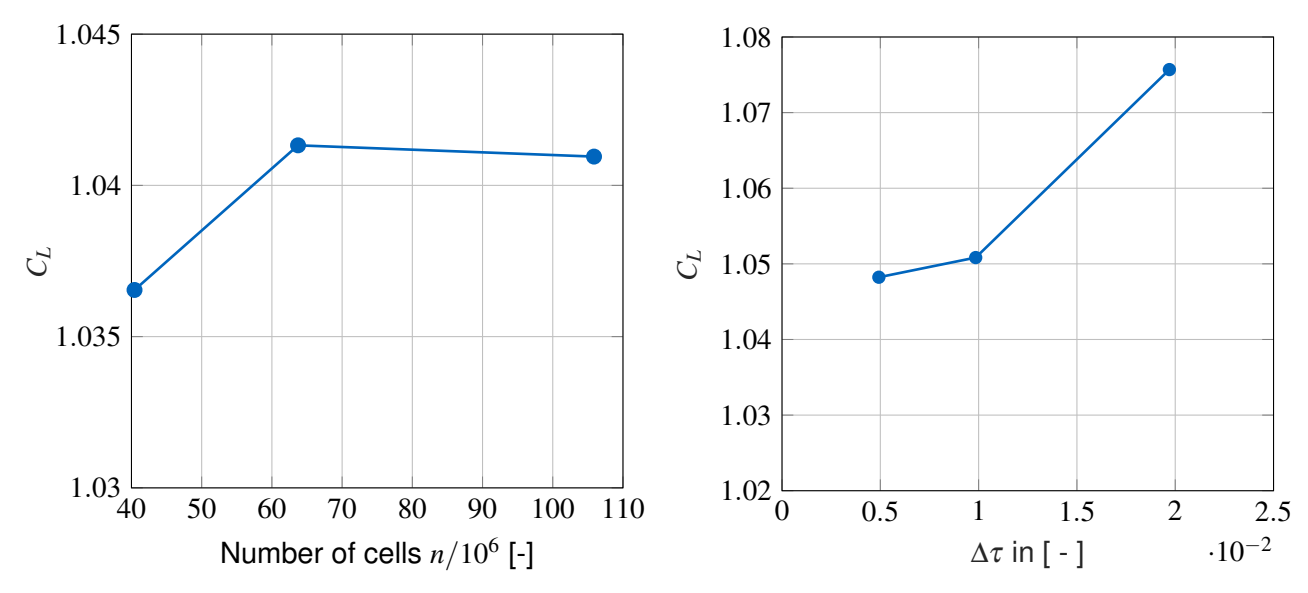
The mesh generation for the fluid domain is based on a hybrid tetrahedral technique. Tetrahedral cells populate exterior regions, while prisms model the boundary layer. A hemispherical pressure far field surrounds the wing, with a diameter of $100 \cdot s$, its flat surface serving as the symmetry plane (xz-plane). Prism layers within the medium grid use a uniform offset method, comprising 30 layers with a final transition ratio of 0.5. Initial layer height is set to $4.00 \times 10^{-6}\,\mathrm{m}$, ensuring proper boundary layer resolution with a maximum y^+ value less than 1. The volume mesh undergoes a systematic grid sensitivity assessment across coarse, medium, and fine refinement levels. The grid sensitivity study (see Figure 6a) is conducted at $\alpha=20^\circ$ and $q/E=0.8\times 10^{-6}$ for pure CFD calculations without the consideration of structural deformations. Here, the time averaged lift coefficient is analyzed over the last 2000 time steps ($\Delta t_s=0.0001\,\mathrm{s}$). The medium grid, with 64×10^6 cells, shows a relative difference below 0.05% with respect to the next finer mesh and is deemed adequately resolved based on this assessment.

A time step sensitivity study for $\alpha=20^\circ$ and $q/E=0.8\times10^{-6}$ and a rigid consideration of the model, depicted in Figure 6b, guides selection of an intermediate time step of $\Delta t_s=0.0001\,\mathrm{s}$ ($\Delta \tau=\Delta t\cdot U_\infty/l_\mu=0.01$), striking a balance between convergence time and result accuracy.

For the coupled CFD and computational structural mechanics (CSM) calculation a dynamic meshing of wing and flap surfaces is utilized to enable coupling with the structural model. The simulation proceeds with 600 time steps at $\Delta t_s = 0.0005\,\mathrm{s}$ for an initial estimation of the aerodynamics and the structural deformation, followed by a refinement to $\Delta t_s = 0.0001\,\mathrm{s}$ for 1000 time steps with 50 inner iterations per physical time step to achieve continuity residual convergence (5 × 10⁻⁵). Averaging over the final 500 time steps ($\Delta t = 0.01\,\mathrm{s}$) yields the time-averaged flow field.

4.2 Structural Dynamics

In the computational structural mechanics (CSM) analysis within ANSYS, the 3D structure of both the wing and flaps are modeled using the transient structural tool. The contact region between the wing's trailing edge and the flaps is considered perfectly bonded. In total, a mesh of $250\,000$ tetrahedral cells is employed for finite element analysis. Specifically, the main wing comprises $220\,000$ elements, while



- (a) Grid sensitivity study of the lift coefficient \mathcal{C}_L for three grid refinement levels
- (b) Time step sensitivity study of the lift coefficient C_L for three refinement levels

Figure 6 – Grid and time step sensitivity study for the *Model53c* at $\alpha = 20^{\circ}$ and $q/E = 0.8 \times 10^{-6}$

each flap is represented by $15\,000$ cells. Similarly to the CFD process, system coupling regions are designated to the surfaces of the wing and flaps, facilitating data exchange between ANSYS Fluent and Transient Mechanical participants.

4.3 System Coupling

The transfer of data between the CFD simulation and the structural simulation is facilitated through the ANSYS system coupling tool and is also referred to as CFD-CSM coupled simulation. At the start of each physical time step, pressure and shear forces from the CFD mesh, encompassing the wing and flaps, are transferred onto corresponding surfaces of the structural mesh. The resultant deformation of the Finite Element Method (FEM) mesh is then conveyed back to the CFD grid, with wing model deformation propagated into the grid's volume mesh. The strong two way coupling requires an implicit update scheme by conducting multiple consecutive exchange cycles between the two participants for each time step until the changes in the flow forces and the structural displacements for the source and target side of the data transfer reach convergence below a convergence criterion of 0.01.

5. Results and analysis

Subsequently, the main focus lies on the evaluation of the experimental results with additional consideration of numerical findings. Hereby, the experimental results enable the validation of the numerical results, while the numerical analysis allow for a detailed investigation of the three dimensional flow pattern above the wing as well as the structural behavior. As a result, a complementary approach using experimental and numerical data is chosen for the flow field and structural analysis.

5.1 Global Force Analysis

At first, this section provides an overview of the aerodynamic characteristics of the *Model53c* wing as obtained from wind tunnel experiments. Initially, the analysis focuses on the global aerodynamic forces, with specific attention to the forces acting on the wing and flaps, while excluding those induced by the fuselage. The lift coefficient dependent on flap angle and the q/E-ratio is depicted in Figure 7. For $\delta=0^\circ$, both q/E-ratios yield congruent curves up to $\alpha=15^\circ$, beyond which the lower q/E-ratio produces higher C_L -values. At $\alpha=25^\circ$, a disparity of $\Delta C_L=0.031$ between the two ratios is observed, attributed to two effects.

Increased wing loading induces a negative twist, diminishing the effective lift coefficient, particularly evident with lower q/E ratios. Additionally, flap-induced lift forces create a hinge moment, uplifting

the flaps and reducing effective flap angles, accentuated with increased loading. The maximum lift coefficient for $\delta=0^{\circ}$ is attained between $\alpha=[24^{\circ},25^{\circ}]$, with visible stall onset at higher angles.

Flap deflection primarily shifts the lift curve slope, with varying stall characteristics. For the positive flap angle $\delta=30^\circ$ a flattening of the lift curve at $C_{L,max}$ and a pronounced post-stall lift loss occur. Furthermore, a difference in lift coefficient with positively deflected flaps is noted between the investigated q/E ratios. In particular, in the low angle of attack region this difference is clearly pronounced and is reduced in the high lift region, where the effectiveness of the slat is reduced due to flow separation. At $\alpha=25^\circ$, the difference between the two lift curves amounts to $\Delta C_L=0.029$.

Adverse effects manifest with $\delta=-30^\circ$ flap angle in the low angle of attack range, yielding negative lift coefficients. For this scenario a moment around the elastic axis is introduced, increasing the wing twist and augmenting the flap deflection. However, as total lift exceeds zero, this effect diminishes, with convergence of the lift curves for the two q/E ratios occurring at $\alpha=15^\circ$. In the post-stall regime ($\alpha>25^\circ$), the curves of the lower q/E ratio generally surpass those of the higher ratio, irrespective of flap deflection angle.

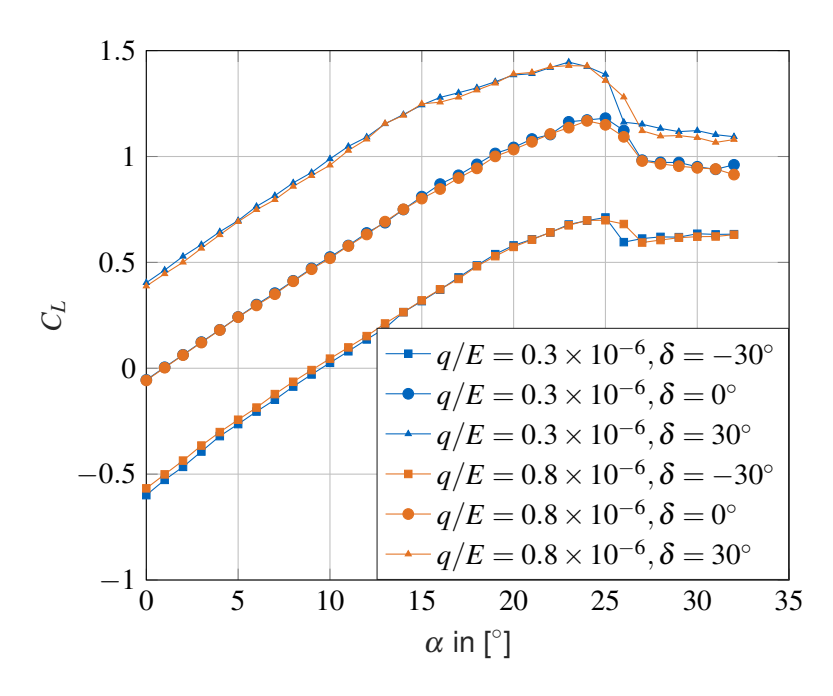


Figure 7 – Lift coefficient C_L over α for three flap angles $\delta = [-30^{\circ}, 0^{\circ}, 30^{\circ}]$ for two q/E ratios

5.2 Flow Field

Following the global aerodynamic analysis, the upcoming sections deal with the local flow pattern of the *Model53c*. Two major vortex systems occur on the wing. One vortex originates from the apex of the wing and is thus referred to as the apex vortex (AV). A second vortex develops on the deployed slat and is called slat vortex (SV). While the experimental results are used for validation purpose, the analysis of the numerical results enables the visualization of more details of the vortex structures, which is depicted in Figure 8. The following cases focus on high angles of attack $\alpha > 20^{\circ}$ where both vortex systems exhibit a burst character over a large portion of the wing.

5.2.1 Mean velocity field

Subsequently, the results of the PIV measurements are investigated for $q/E=0.3\times 10^{-6}$ to analyze the basic characteristics of the vortex structures. Therefore, the nondimensional axial velocity U/U_{∞} is plotted at two different cross flow planes $x/l_{\mu}=[0.587,0.978]$ for three flap deflection angles ($\delta=[-30^{\circ},0^{\circ},30^{\circ}]$). An angle of attack of $\alpha=20^{\circ}$ is used for this investigation.

Figure 9a shows the according PIV results at the cross flow plane $x/l_{\mu}=0.587$. For a negative flap deflection of $\delta=-30^{\circ}$ a minimum axial velocity of $U/U_{\infty}=0.07$ occurs in the apex vortex core. An increase of the flap angle to $\delta=0^{\circ}$ increases the core velocity to $U/U_{\infty}=0.21$. Additionally, the high

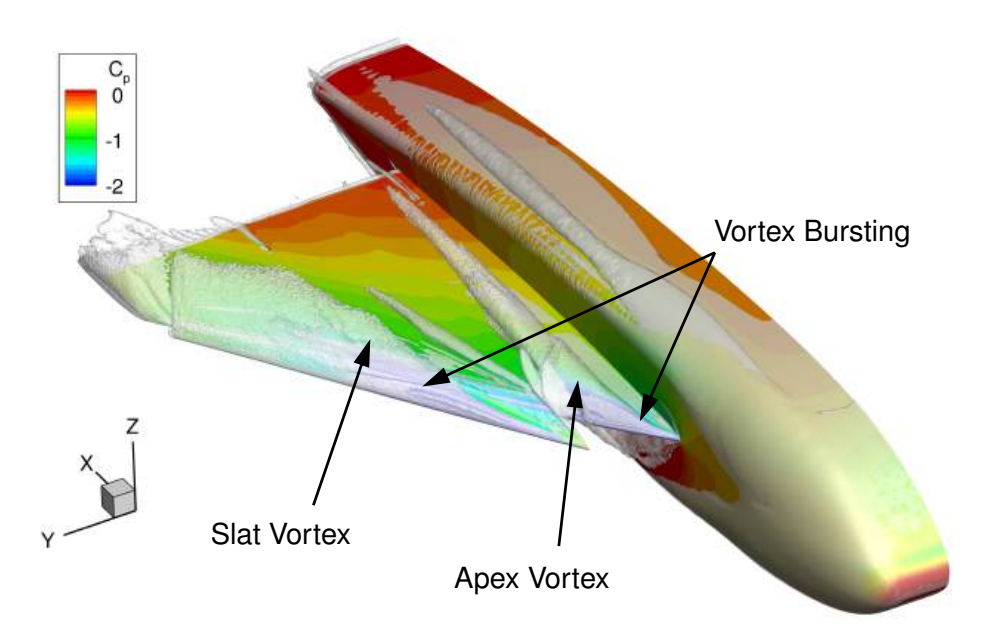


Figure 8 – CFD results: Iso surface for raw Q-criterion ($Q=100\,000\,1/\mathrm{s}^2$) and pressure coefficient distribution averaged over 500 time steps for $\delta=0^\circ$ and $q/E=0.3\times10^{-6}$

velocity region near the slat is expanded. Increasing the flap angle even further to $\delta=30^\circ$ leads to a slight raise of the axial core velocity of the apex vortex to $U/U_\infty=0.23$. The influence region of the slat vortex is again increased. It is noticeable that the size of the apex vortex however is not influenced by the flap deflection. Also its axis location at y/s=0.175 is unaltered.

The aft cross flow plane at $x/l_{\mu}=0.978$, depicted in Figure 9b, shows the apex vortex and the developed slat vortex. For $\delta=-30^{\circ}$ the apex vortex exhibits a minimum axial velocity of $U/U_{\infty}=0.28$ in its core, surrounded by a large low velocity region $(U/U_{\infty}<0.6)$ with a diameter of $0.2 \cdot s$. By increasing the flap angle to $\delta=0^{\circ}$ the nondimensional axial velocity increases to $U/U_{\infty}=0.45$ and the core velocity is increased further to $U/U_{\infty}=0.56$ for $\delta=30^{\circ}$. Simultaneously, the region of low velocity surrounding the core shrinks down. Like for the upstream cross flow plane the location of the vortex core is unaffected by the flap position (y/s=0.19). Regarding the apex vortex no significant increase of the size of the low velocity region is identified between the upstream and the downstream cross flow plane.

Between $0.4 \cdot s - 0.5 \cdot s$ a small vortical structure, which is called the midboard vortex (MBV), is identified, that originates from the inboard section of the slat. The size of this small scale vortex structure is effected by the SV, which suppresses the MBV with increased flap angle.

For the slat vortex an increase of the flap angle shifts the vortex axis further inboard and upwards. Additionally, an increased flap angle reduces the minimum velocity in the core of the vortex. Contrary to the apex vortex, an increase of the flap deflection angle leads to a reduction of the core velocity. For $\delta = -30^{\circ}$, a minimum core velocity of $U/U_{\infty} = 0.17$ is reached in the slat vortex. The zero flap deflection leads to a reduced core velocity of $U/U_{\infty} = 0.14$, while the vortex axis is located at y/s = 0.67. At the most positive flap deflection ($\delta = 30^{\circ}$) a reversed flow region occurs in the core with $U/U_{\infty} = -0.02$. Furthermore, increasing the flap angle also increases the size of the low velocity region surrounding the core.

Regarding the undeflected flap deflection the computational results are presented in Figure 10a. Here, a cross flow plane at $x/l_{\mu}=0.978$ is investigated regarding the mean normalized axial velocity field. A low velocity region is identified in the AV core with a nondimensional velocity of $U/U_{\infty}=0.68$, which is increased with respect to the PIV measurements. The apex core is positioned at y/s=0.19. The SV core exhibits a low velocity region in the core with $U/U_{\infty}=0.07$. Its core is located at y/s=0.66. The low velocity region of the slat vortex expands further inboard with respect to the experimental results. The results of the numerical analysis show that both vortices exhibit a burst character. This is also visualized in Figure 8, where the bursting point of the AV occurs between

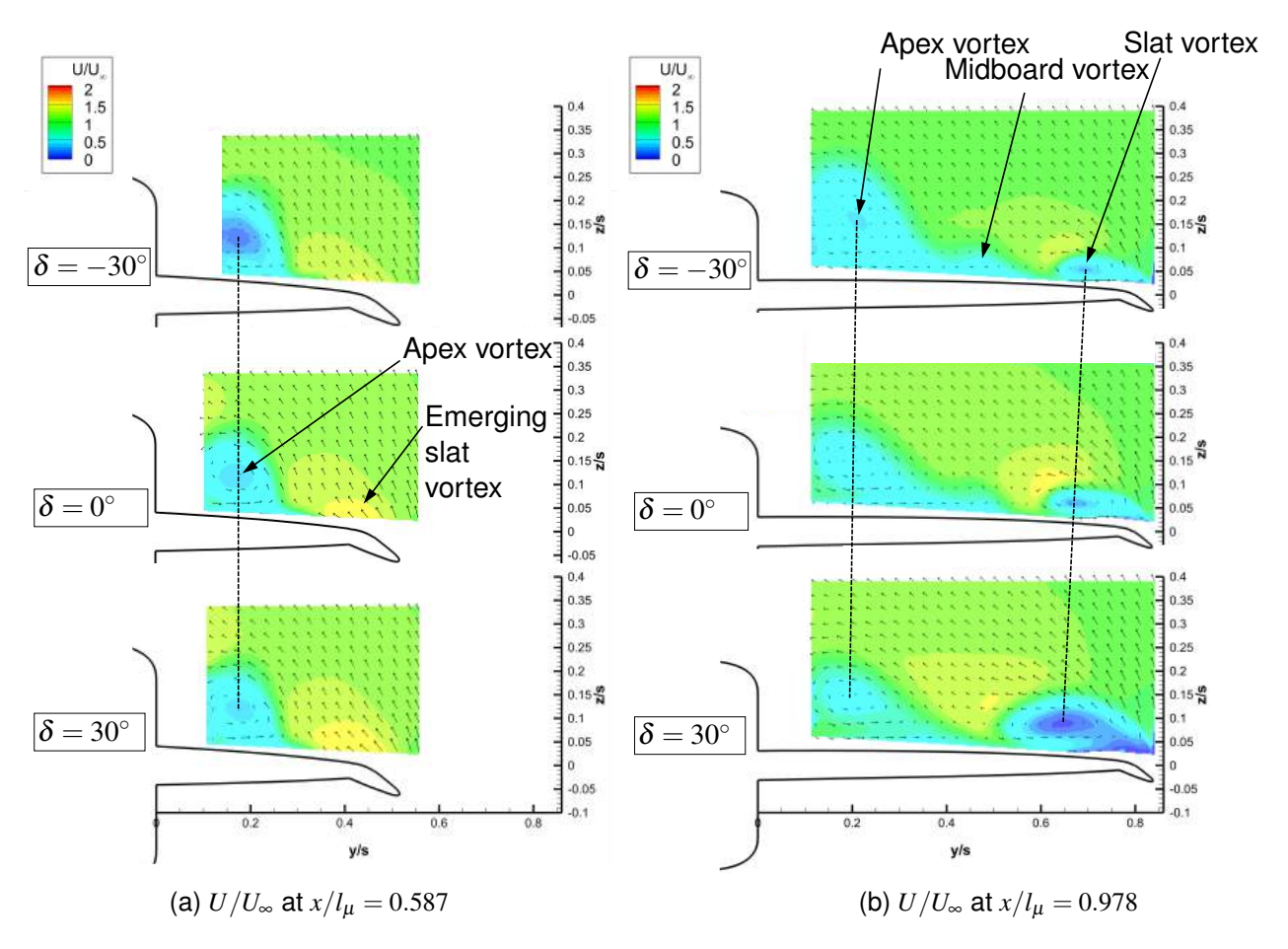


Figure 9 – U/U_{∞} distribution and velocity vector field for three flap angles at $\alpha=20^{\circ}$ and $q/E=0.3\times10^{-6}$

 $x/l_{\mu} = [0.078, 0.098]$ and for the SV between $x/l_{\mu} = [0.587, 0.685]$.

The influence of an increased angle of attack α on the vortex structure has also been studied during the experimental measurements and is shown in Figure 11. Similar to Figure 9, the location of the axis of the apex vortex is not affected by the flap deflection. However, the increased angle of attack causes an increase of the slat vortex size. Additionally, its vortex core is shifted upwards and inboard with respect to $\alpha=20^\circ$. As a result, the low velocity regions of the apex and the slat vortex start to merge. A large reversed flow area dominates the center of the slat vortex. As for $\alpha=20^\circ$, an increase of the flap deflection angle shifts the slat vortex core further inboard.

For all investigated flap angles δ and angles of attack α , the velocity vector field in the cross flow planes show a low angular velocity in the vortex cores and higher angular velocities outside the core region, which also indicates a burst vortex structure.

5.2.2 Unsteady Velocity Fields

Following, the PIV results are complemented by the FRAP results for a q/E ratio of 0.3×10^{-6} . Therefore, locations with high normalized turbulent kinetic energy gradient are chosen as a region of interest for the transient flow evaluation. The normalized turbulent kinetic energy (TKE) is calculated in Equation 1, with the corresponding turbulence intensity I being outlined in Equation 2.

$$TKE = \frac{u_{rms}^2 + v_{rms}^2 + w_{rms}^2}{2 \cdot U_{\infty}^2} \tag{1}$$

$$I = \sqrt{\frac{2}{3} \cdot TKE} \tag{2}$$

The evaluation of the transient data, gathered by the FRAP measurements, is visualized by a Power Spectral Density (PSD) plot of the fluctuations of the mean pressure coefficient at all five sensors

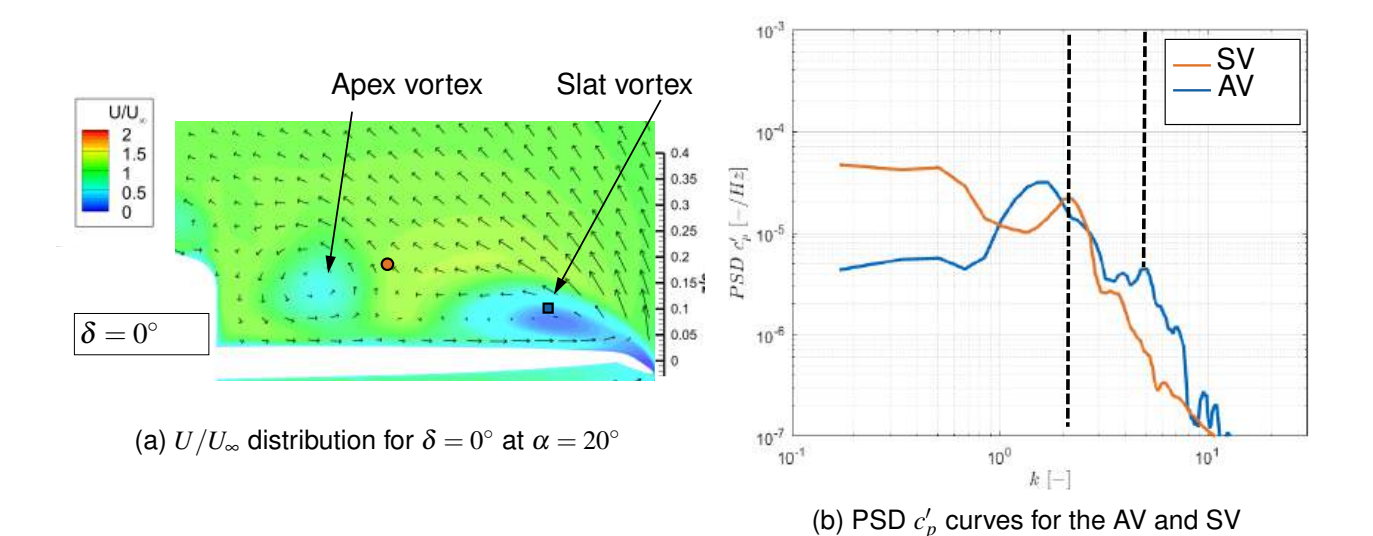


Figure 10 – U/U_{∞} distribution and PSD c_p' analysis for $\delta=0^{\circ}$ at $\alpha=20^{\circ}$, $q/E=0.3\times10^{-6}$ and $x/l_{\mu}=0.978$

Angle of attack	x/l_{μ}	k_H
$lpha=20^\circ$	0.196	5.06 - 6.05
	0.587	1.69 - 2.02
	0.979	1.01 - 1.21
$\alpha = 25^{\circ}$	0.196	4.09 - 4.89
	0.587	1.36 - 1.63
	0.979	0.82 - 0.98

Table 6 – Estimated frequency ranges of the HMI with no slat influence ($\theta = 0$)

of the probe. The PSD values are plotted over the reduced frequency $k = \frac{f \cdot l_{\mu}}{U_{\infty}}$. With the PIV data analyzed, the AV and the SV have been identified to exhibit a burst characteristic at $x/l_{\mu} = 0.587$ and $x/l_{\mu} = 0.979$. Associated to vortex bursting for this application is the helical mode instability (HMI). A prediction of the dominant reduced frequency k of a HMI based on empirical data has been conducted in [23] and adapted in [24] for double and triple delta wings. This paper includes a modification of the prediction method as the original approach does not include the influence of a deployed slat. A correction angle θ (see Equation 4) is introduced in Equation 3 to account for the influence of the slat at a certain location in span and chord wise direction as depicted in Figure 12. The correction angle θ is calculated considering the slat deflection angle δ_S , the slat length percentage with respect to the local chord length at a given point p(x,y) and relative distance c_{rel} of this point p to the leading edge with respect to the local chord length. The estimation of the occurring HMI at certain angles of attack and positions on the wing are give in Table 6 and 7 with and without the consideration of the slat influence.

$$k_H = \frac{l_{\mu}}{x} \cdot \frac{1}{\cot(\varphi_{LE}) \cdot \sin(\alpha - \theta)} \cdot (0.28 \pm 0.025)$$
(3)

Angle of attack	x/l_{μ}	y/s	k_H
$lpha=20^\circ$	0.979	0.63	1.89 - 2.26
$\alpha=25^{\circ}$	0.979	0.63	1.29 - 1.54

Table 7 – Estimated frequency ranges for the HMI with influence of a deployed slat ($\theta = 9.45^{\circ}$)

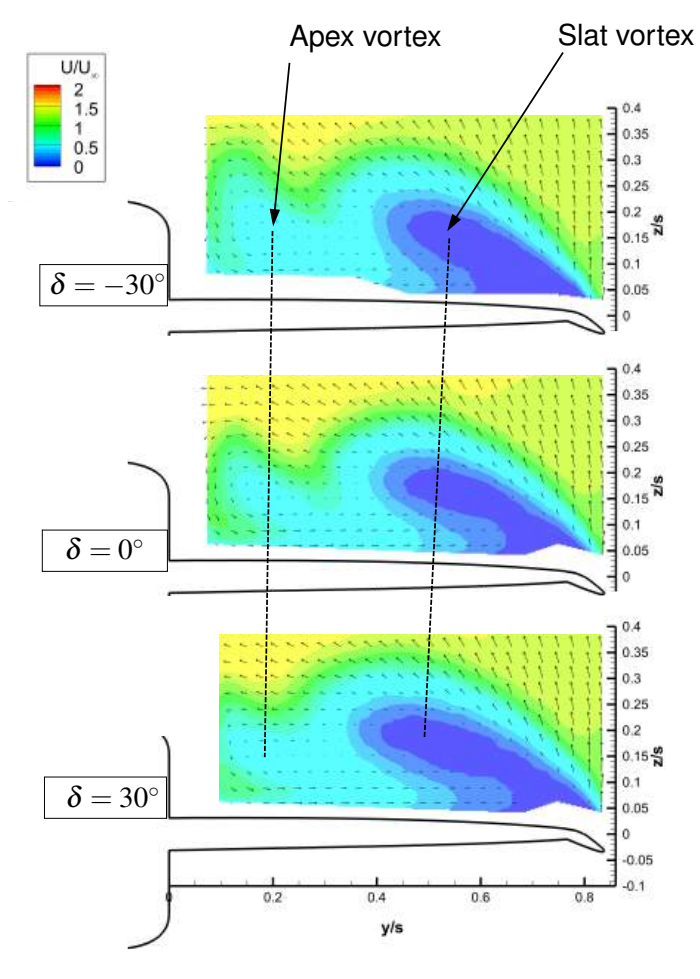


Figure 11 - U/U_{∞} distribution and velocity vector field for three flap angles at $\alpha=25^{\circ}$, $x/l_{\mu}=0.978$ and $q/E=0.3\times10^{-6}$

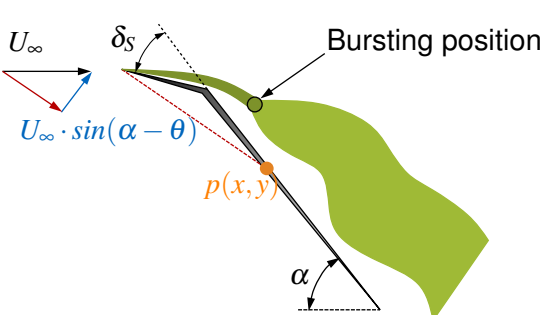


Figure 12 – 2D schematic representation of dominant buffet phenomena with deployed leading edge slat, adapted from [23] at a chord section of a delta wing

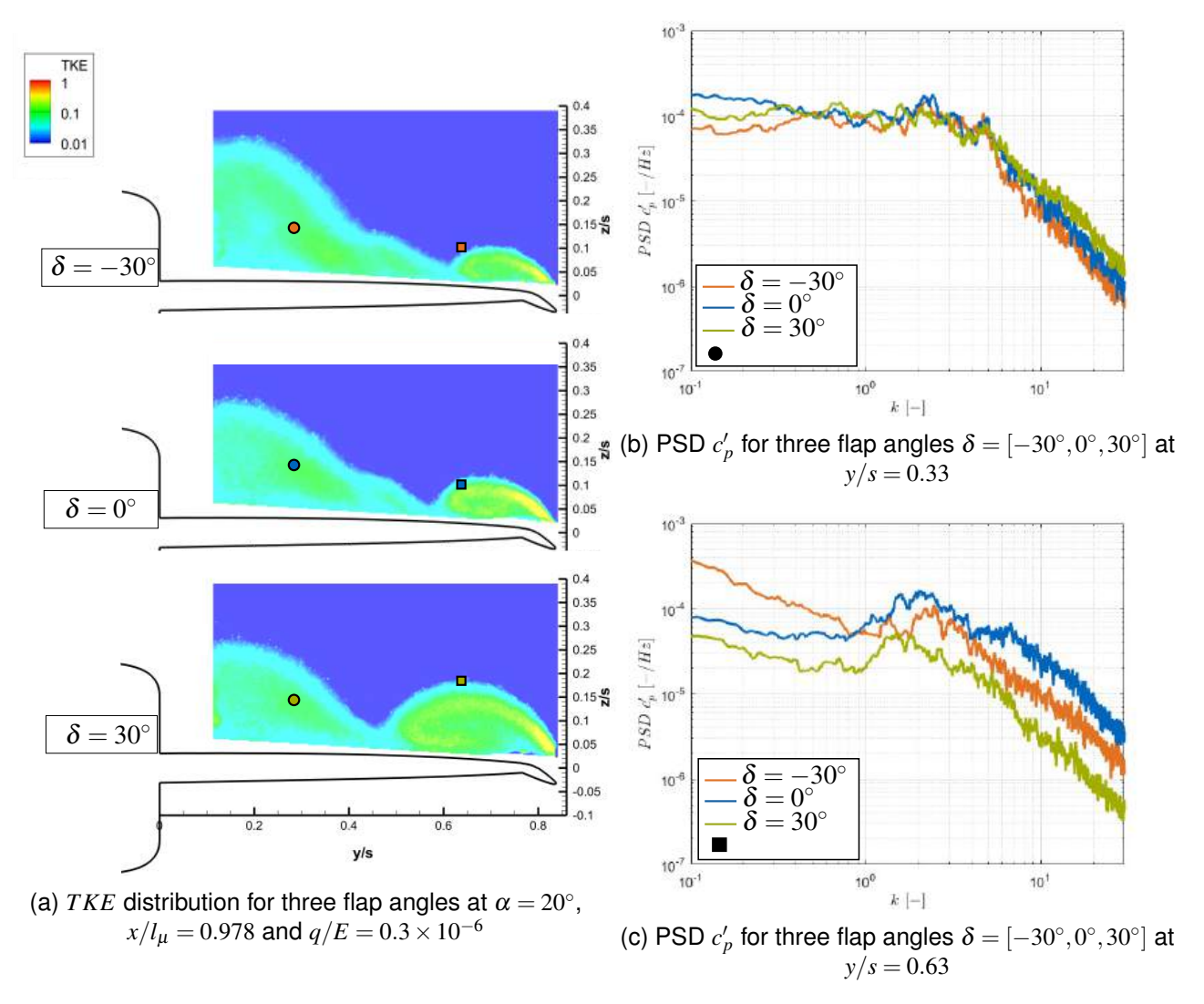


Figure 13 – TKE distribution and PSD analysis for three flap angles at $\alpha=20^\circ, x/l_\mu=0.978$ and $a/E=0.3\times10^{-6}$

$$\theta = \arctan(\frac{\tan(\delta_S) \cdot c_{S,rel}}{c_{rel}(x, y)})$$
(4)

Figure 13 shows the TKE distribution at $x/l_{\mu}=0.978$ and an angle of attack of $\alpha=20^{\circ}$ for three different flap positions as well as the transient data for one point in the influence region of the AV and the SV. The TKE distribution in Figure 13a allows the identification of the highly turbulent shear layer of the SV (TKE=[0.1,0.3]) corresponding to turbulence intensities I=[25%,45%]. A region of high TKE gradients close to the shear layer of the SV at y/s=0.63 is investigated regarding the PSD of the pressure fluctuations c'_p in Figure 13c. A broadband local maximum of the PSD c'_p values for $\delta=0^{\circ}$ occurs in the reduced frequency range of k=[1.9,2.3]. This local maximum in the recorded pressure coefficient fluctuations corresponds to a helical mode instability (HMI) of the slat vortex. The predicted reduced frequency of the HMI in Table 7 delivers a value k=[1.89-2.26]. Reducing the flap deflection angle to $\delta=-30^{\circ}$ shifts the maximum of the PSD c'_p distribution to a higher frequency of k=2.4. Contrary to that, for $\delta=30^{\circ}$ the dominant frequency is reduced to k=1.5, indicating an increased wavelength of the instability mode and thus a larger diameter of the slat vortex with respect to the undeflected flaps.

The influence region of the AV is characterized by moderate TKE values of TKE < 0.1 (I < 25%). Similar as for the SV a measurement point is chosen in a region of high TKE gradients at y/s = 0.33. For the AV two dominant frequencies can be identified in the PSD u'/U_{∞} plot (see Figure 13b) for

all three cases. A HMI occurs for k = [4.5 - 4.9] for all investigated flap angles. The flap deflection has no effect on the occurring dominant frequency. A second peak at k = [2.2 - 2.6] can be identified for all flap angles. This frequency corresponds to a vortex structure originating from the intersection between the slat and the inboard wing section.

Considering the transient results of the numerical investigation enables a comparison regarding the dominant frequencies of the PSD c_p' curves. In that regard, the power spectral density analysis of the static pressure coefficient fluctuations at a point in the close vicinity of the AV and the SV is conducted for $\alpha=20^\circ$, $x/l_\mu=0.978$ and $q/E=0.3\times10^{-6}$. An evaluation of the fluctuation near the AV and the SV is presented in Figure 10b. For the SV a maximum in the PSD c_p' curve occurs at k=2.2, which complies with the analytically predicted values from Table 7 and the FRAP results. Both distinct peaks for the AV can be identified for the simulation results as well. A low frequency peak appears at k=1.7, while a high frequency peak is visible at k=4.9.

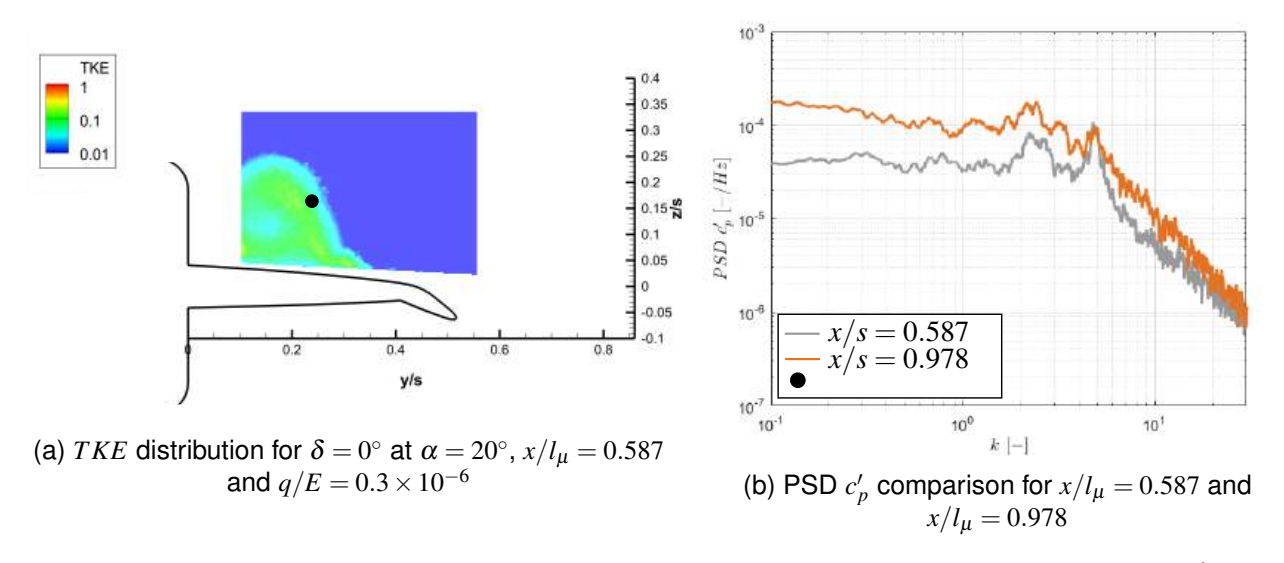
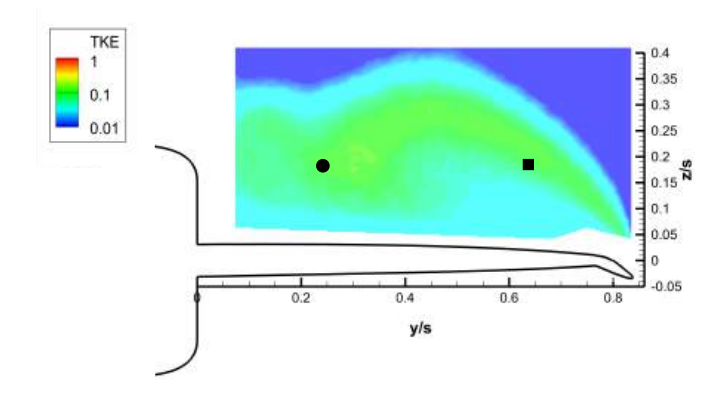


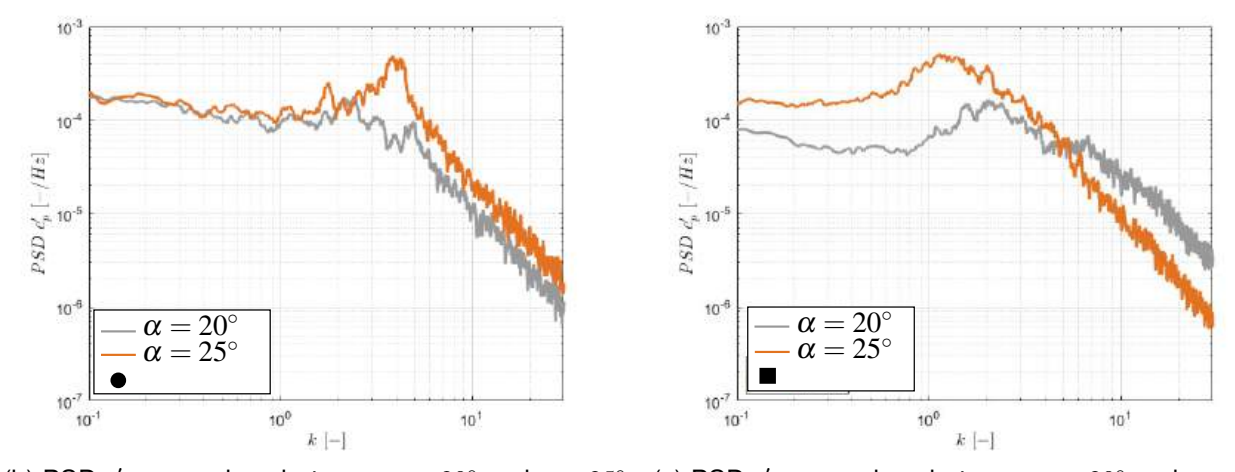
Figure 14 – TKE distribution and PSD c_p' analysis for $\delta=0^\circ$ at $\alpha=20^\circ$, $q/E=0.3\times10^{-6}$ and $x/l_\mu=0.587$

Figure 14 shows the experimental results for TKE distribution and PSD c_p' curves at a distinct point in the outer layer of the AV at $x/l_\mu=0.587$ for undeflected flaps. The TKE distribution in Figure 14a shows an annular ring of higher TKE values (TKE=[0.09-0.13]) and a low TKE region in the core (TKE<0.05 and I<18%) confirming the already burst character of the AV. A point at y/s=0.24 close to the high TKE region of the annular ring is used for the evaluation of the PSD c_p' data. Figure 14b visualizes the PSD data for $x/l_\mu=0.587$ and $x/l_\mu=0.978$. Both curves exhibit dominant frequencies at k=[2.2-2.6] and k=[4.5-4.85] as described above. These results are in accordance with the results depicted in Figure 9. There, it was concluded that the flow pattern of the AV shows no increase in size between the cross flow plane $x/l_\mu=0.587$ and $x/l_\mu=0.978$. This is due to the deployed slat which prevents a further feeding of the AV downstream of $x/l_\mu=0.196$ where the slat is deployed. As a result, the dominant frequency for the AV is almost unaffected downstream of $x/l_\mu=0.196$ and can be approximated by using Equation 3 with $\theta=0^\circ$ and $x/l_\mu=0.196$. Table 6 shows a minor over prediction of the frequency of the HMI for $x/l_\mu=0.196$ and $\alpha=20^\circ$ at k=[5.06-6.06].

The influence of a lager angle of attack of $\alpha=25^\circ$ at $x/l_\mu=0.978$ and undeflected flaps for the experimental setup is described in Figure 15. The TKE distribution, shown in Figure 15a, highlights a large influence zone of the slat vortex that takes three quarters of the according wing section. The SV starts to merge with the AV at y/s=0.2. Additionally, the influence region of the SV reaches up to z/s=0.375. A comparison of the PSD c_p' curves between $\alpha=20^\circ$ and $\alpha=25^\circ$ at y/s=0.63 is depicted in Figure 15c. As shown before, the dominant frequency of the SV at $\alpha=20^\circ$ occurs at k=[1.9,2.3]. For the increased angle of attack of $\alpha=25^\circ$ the dominant frequency is shifted to lower values between k=[1.1-1.5] as predicted in Table 7. A similar observation is made for the AV. Here, the frequency of the dominant peak in the PSD c_p' curve is shifted from k=[4.5-4.9] to k=[3.8-4.1]



(a) TKE distribution for $\delta=0^{\circ}$ at $\alpha=25^{\circ}$, $x/l_{\mu}=0.978$ and $q/E=0.3\times10^{-6}$



(b) PSD c_p' comparison between $\alpha=20^\circ$ and $\alpha=25^\circ$ (c) PSD c_p' comparison between $\alpha=20^\circ$ and $\alpha=25^\circ$ for the SV

Figure 15 – TKE distribution and PSD c_p' analysis for $\delta=0^\circ$ at $\alpha=25^\circ$ and $q/E=0.3\times10^{-6}$

confirming the predicted data from Table 6 for $x/l_{\mu} = 0.196$ (k = [4.09 - 4.89]).

The findings of the dominant buffet frequencies is hereby of major importance for future structural analysis. In particular, with regard to the first three eigenfrequencies of the structural model, lying at $f = [35\,\mathrm{Hz}, 90\,\mathrm{Hz}, 104\,\mathrm{Hz}]$, which corresponds to reduced frequencies k = [0.59, 1.53, 1.76]. As shown previously, those reduced structural frequencies lie in a similar range as the broadband spectrum of the SV instability mode for the discussed conditions, which is a supporting requirement to trigger buffeting.

5.3 Deformation Analysis

Following the results of the aerodynamic analysis, the photogrammetry measurements are investigated. The effect of the flap deflection is analyzed by comparing the deformation of the wing at $\alpha=20^\circ$ and $q/E=0.3\times10^{-6}$ for the three flap angles aforementioned. The total deformation ε is calculated according to Equation 5.

$$\varepsilon = \sqrt{\Delta x^2 + \Delta y^2 + \Delta z^2} \tag{5}$$

Figure 16 illustrates the corresponding nondimensional deformation ε/s for the three different flap deflections. The deformation shape of the wing surface with $\delta=0^\circ$ and $\delta=30^\circ$ exhibit a high degree of similarity, with the most notable differences in the magnitude of deformation in proximity of the tip and the flap surface. The maximum nondimensional deformation for $\delta=0^\circ$ amounts to $\varepsilon/s=0.007$ while the maximum value for $\delta=30^\circ$ is $\varepsilon/s=0.011$. The largest contribution to the wing deformation results from the first bending mode of the wing model as determined in previous studies (see [16]). The *Model53c* experiences an upward bending deformation with increasing magnitude towards the wing tip. This is coupled with a torsional deformation which reduces the local twist angle and thus

EXPERIMENTAL AND NUMERICAL INVESTIGATION OF A STRUCTURAL-DYNAMICALLY SCALED DELTA WING

the effective angle of attack, particularly pronounced at the wing tip. Conversely, the wing surface for $\delta=-30^\circ$ exhibits an additional contribution of the twisting mode (see [16]), with a less pronounced bending deformation as for higher flap deflection angles. The torsional deformation for this configuration leads to an increase of the local twisting angle with respect to higher flap deflection angles and thus to an increase of the effective angle of attack, in particular, in the section close to the wing tip. The maximum deformation of the wing is reduced to $\varepsilon/s=0.003$.

Thus, the flaps majorly influence the twist behavior of the wing. A positive flap deflection reduces the twist deformation, while a negative flap deflection increases it. The detailed insight into the twist distribution for the three flap deflection angles is given in Figure 18. For undeflected flaps, the wing twist is reduced with respect to the undeformed wing. In particular in the tip region, the change in twist reaches a minimum value $\Delta\theta=-0.28^\circ$. A positive flap deflection increases the downward twist of the wing further resulting in $\Delta\theta=-0.68^\circ$ in the tip region. As already seen in Figure 16, the negative flap deflection introduces a minor positive twist. The according change in the twist distribution is pictured in Figure 18. The change in the twist distribution starts to level out at y/s=0.655 and reaches a maximum value of $\Delta\theta=0.15^\circ$ at y/s=0.92.

Due to the influence of the induced twist under loading, the positive and undeflected flap deflection reduces the local angle of attack in particular in the outboard wing section, while the negative flap deflection slightly increases the local angle of attack.

Regarding the numerical analysis, the case for undeflected flaps is further investigated for the wing at $\alpha=20^\circ$ and $q/E=0.3\times10^{-6}$. The deformation is depicted in Figure 17. As for the potogrammetry results, the bending deformation of the wing dominates the total deformed shape. In the tip region a maximum deformation of $\varepsilon/s=0.006$ occurs, exhibiting a minor under prediction with respect to the photogrammetry results ($\varepsilon/s=0.007$). The evaluation of the change in the twist distribution, given in Figure 18, shows a similar course for the experimental and the numerical results. For the numerically

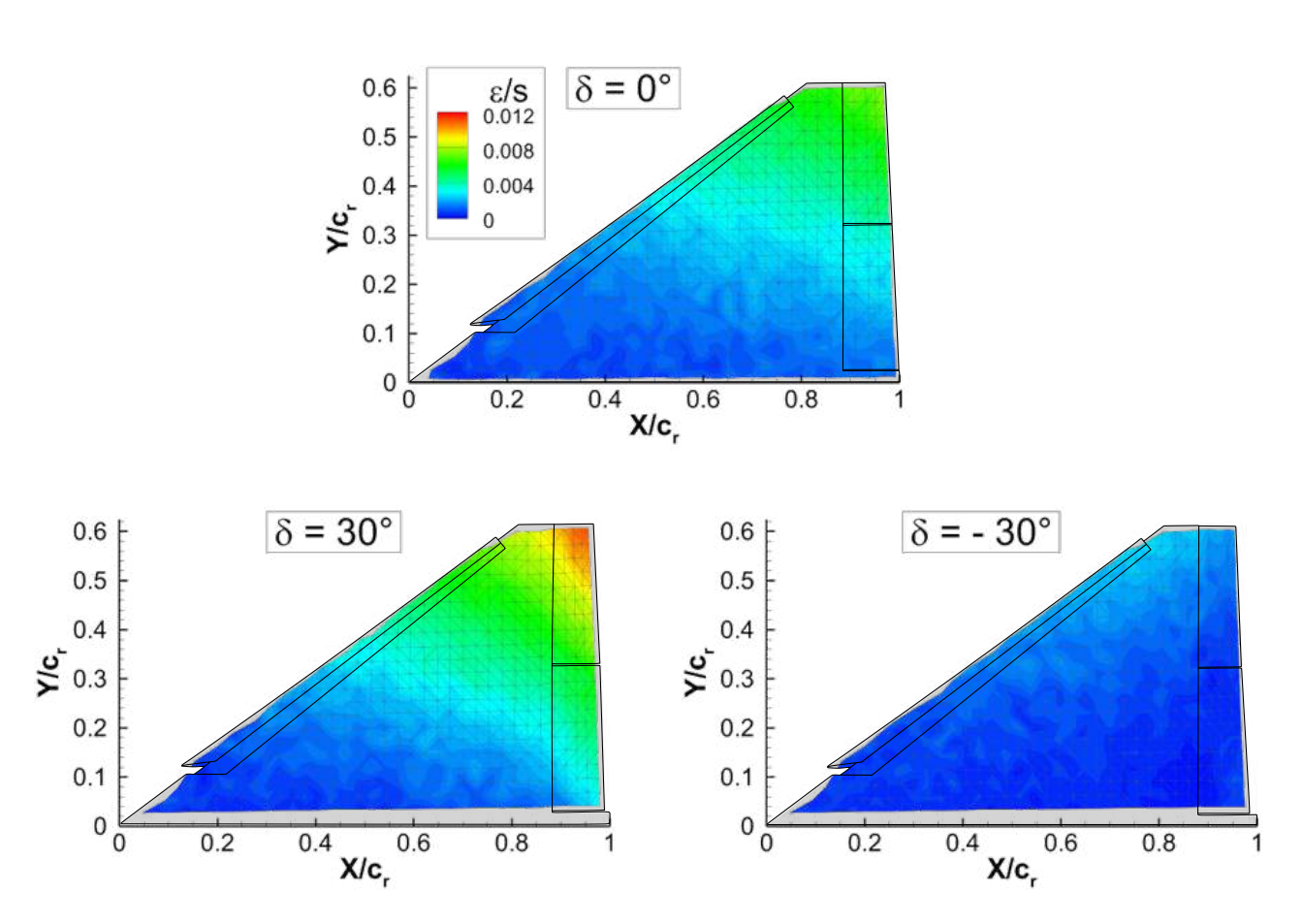


Figure 16 – Nondimensionalised deformation ε/s at $\alpha=20^\circ$ at the q/E-ratio of $q/E=0.3\times 10^{-6}$ for three flap angles $\delta=[-30^\circ,0^\circ,30^\circ]$

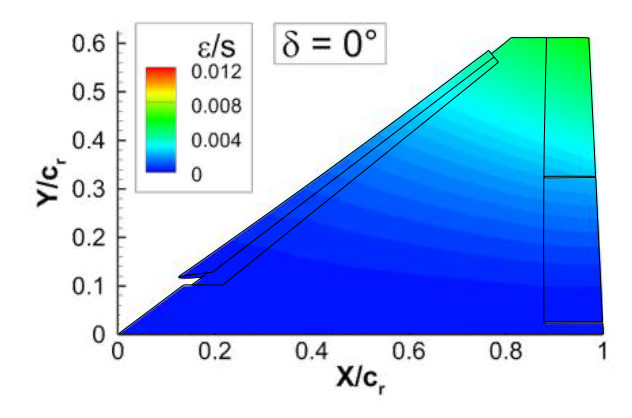


Figure 17 – Simulation results for nondimensionalised deformation ε/s at $\alpha=20^\circ$ at the q/E-ratio of $q/E=0.3\times 10^{-6}$ for undeflected flaps

determined change in twist $\Delta\theta$ a discontinuity in the curve can be detected at y/s=0.5, where a gap between the two flaps occurs. The jump in $\Delta\theta$ indicates a stronger impact of the outer flap section to the twist deformation compared to the inner flap. A maximum value of $\Delta\theta=-0.21^\circ$ is present at the tip.

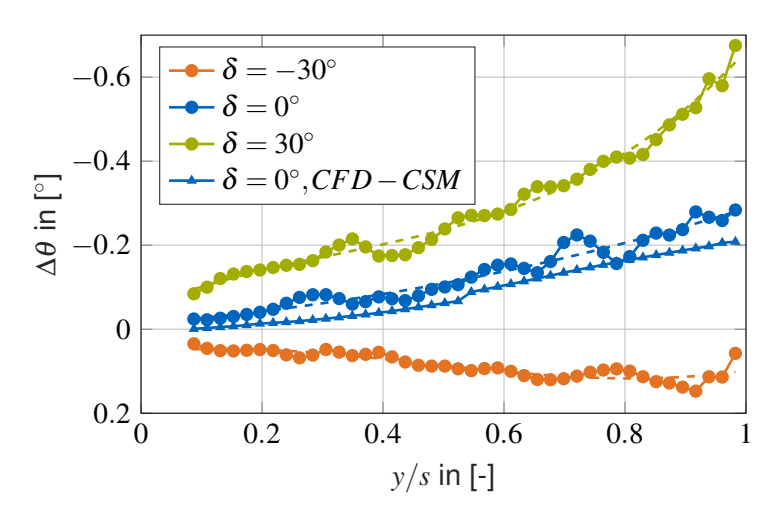


Figure 18 – Wing twist distribution over y/s for three flap deflection angles at $\alpha=20^\circ$ and $q/E=0.3\times10^{-6}$

6. Conclusion

This study focuses on examining an aeroelastically designed delta wing through both experimental and computational analysis. Wind tunnel tests were conducted to explore the overall and local aerodynamic behaviors under various inflow conditions and with varying flap angles. The examination of force data for two distinct q/E ratios confirmed the anticipated responses concerning model deformation. The PIV analyses enabled the identification of the vortical flow structure for the apex vortex and the slat vortex as well as the development for a change of the flap angle and the angle of attack. It is noted that an increase of the flap angle increases the diameter of the slat vortex. Simultaneously, the vortex axis of the slat vortex is shifted further inboard and upwards. The vortex axis of the apex vortex shows minor dependency on the flap position. An increase of the angle of attack, in particular, lead to a growing reversed flow region for the slat vortex. Analyzing the transient characteristics of the flow field, by applying the FRAP measurement, shows a different characteristic of the apex vortex and the slat vortex. For the apex vortex a change of the flap deflection shows no significant impact on the dominant frequency of the vortex system. Furthermore, due to the deflected slat, the feeding of the apex vortex is suppressed downstream $x/l_{\mu}=0.196$ which leads to no significant shift of the dominant frequencies to lower values for further downstream located cross flow planes. The dominant

EXPERIMENTAL AND NUMERICAL INVESTIGATION OF A STRUCTURAL-DYNAMICALLY SCALED DELTA WING

frequency of the slat vortex, however, is affected by the flap deflection. Increasing the flap deflection angle shifts the dominant frequencies to lower values. Additionally, an analysis of the time resolved pressure fluctuations near the apex vortex and the slat vortex showed proper accordance of the analytical with experimental prediction of dominant frequencies. Apart from the aerodynamic analyses, the structural deformation of the delta wing is measured. The results show a significant influence of the flap angle on the total deflection of the wing. Positive and negative flap deflections exhibit a different shape of the deformation, in particular, as far as the rotated axis for the bending motion of the wing is concerned. Furthermore, the induced twist angle increases with a reduction of the flap angle. Finally, the experimental results are compared to numerical calculations. In that regard, the $\mathit{Model53c}$ is investigated at $\alpha=20^\circ$ and $q/E=0.3\times10^{-6}$ with undeflected flaps. The aerodynamic analysis of the apex vortex shows a high order of similarity with respect to the experimental data set. The size of the slat vortex is over predicted by the simulation. By analyzing the numerical results of the structural deformation of the $\mathit{Model53c}$ it is spotted that the wing bending and twist comply with the findings of the experiments.

For the next phase of the study, a further computational insight in the aerodynamic and structural phenomena of the delta wing will be conducted. Therefore, multiple flap deflection angles as well as scale resolving simulations will be subject to the analysis.

7. Contact Author Email Address

konstantin.bantscheff@tum.de

8. Acknowledgments

The authors want to thank ANSYS for providing the simulation software used for the numerical investigations and the Gauss Centre for Supercomputing e.V. (www.gausscentre.eu) for funding this project by providing computing time on the GCS Supercomputer SuperMUC at Leibniz Supercomputing Center (LRZ, www.lrz.de).

9. Copyright Statement

The authors confirm that they, and/or their company or organization, hold copyright on all of the original material included in this paper. The authors also confirm that they have obtained permission, from the copyright holder of any third party material included in this paper, to publish it as part of their paper. The authors confirm that they give permission, or have obtained permission from the copyright holder of this paper, for the publication and distribution of this paper as part of the ICAS proceedings or as individual off-prints from the proceedings.

References

- [1] C. Breitsamter. *Turbulente Strömungsstrukturen an Flugzeugkonfigurationen mit Vorderkantenwirbeln*. Aerodynamik. Utz, Herbert, Dissertation, Munich, Germany, 1997.
- [2] D. Hummel and G. Redeker. Experimentelle bestimmung der gebundenen wirbellinien sowie des strömungsverlaufs in der umgebung der hinterkante eines schlanken deltaflügels. *Abhandlungen der Braunschweigischen Wissenschaftlichen Gesellschaft*, 1:273–290, 1971.
- [3] N. G. Verhaagen, L.N. Jenkins, and S. Kern. A study of the vortex flow over 76 / 40-deg double-delta wing. NASA Contractor Report 195032, 1995.
- [4] A. Schütte and D. Hummel. Numerical design studies on the roll stability of a multi-delta-wing configuration. *Journal of Aircraft*, 60(3):898–914, 2023.
- [5] J. Cai, S. Pan, W. Li, and Z. Zhang. Numerical and experimental investigations of a nonslender delta wing with leading-edge vortex flap. *Computers and amp Fluids*, 99:1–17, 2014.
- [6] L. W. Traub. Experimental investigation of the effect of trailing-edge flaps on delta wings. *Journal of Aircraft*, 54(5):1945–1959, 2017.
- [7] D. G. Mabey. Some aspects of aircraft dynamic loads due to flow separation. *Progress in Aerospace Sciences*, 26(2):115–151, 1989.
- [8] G. Stenfelt and U. Ringertz. Design and construction of aeroelastic wind tunnel models. *The Aeronautical Journal*, 119(1222):1585–1599, 2015.
- [9] F. W Gibson and W. B. Igoe. Measurements of the buffeting loads on the wing and horizontal tail of a 1/4-scale model of the x-1e airplane. *Report NASA Research Memorandum L57E15*, 1957.

EXPERIMENTAL AND NUMERICAL INVESTIGATION OF A STRUCTURAL-DYNAMICALLY SCALED DELTA WING

- [10] N. Khan, V. Acanfora, and A. Riccio. Non-conventional wing structure design with lattice infilled through design for additive manufacturing. *Materials*, 17(7):1470, 2024.
- [11] N. Tsushima, K. Saitoh, and K. Nakakita. Structural and aeroelastic characteristics of wing model for transonic flutter wind tunnel test fabricated by additive manufacturing with alsi10mg alloys. *Aerospace Science and Technology*, 140:108476, 2023.
- [12] S. K. Chimakurthi, S. Reuss, M. Tooley, and S: Scampoli. ANSYS workbench system coupling: a state-of-the-art computational framework for analyzing multiphysics problems. *Engineering with Computers*, 34(2):385–411, 2017.
- [13] L. Zhang and C. Sun. Simulation analysis of fluid-structure interaction of high velocity environment influence on aircraft wing materials under different mach numbers. *Sensors*, 18(4):1248, 2018.
- [14] P. J. Attar, R. E. Gordnier, and M. R. Visbal. Numerical simulation of full-span delta wing buffet at high angle of attack. *Journal of Aircraft*, 45(3):857–867, 2008.
- [15] C. Katzenmeier, L.and Vidy, A. Kolb, and C. Breitsamter. Aeroelastic wind tunnel model for tail buffeting analysis using rapid prototyping technologies. *CEAS Aeronautical Journal*, 12(3):633–651, 2021.
- [16] K. Bantscheff and C. Breitsamter. Dynamic structural scaling concept for a delta wing wind tunnel configuration using additive manufacturing. *Aerospace*, 10(7):581, 2023.
- [17] Formlabs. Validierung von Isotropie beim SLA 3D-Druck formlabs.com. https://formlabs.com/de/blog/validierung-von-isotropie-beim-sla-3d-druck. [Accessed 15-Feb-2023].
- [18] Accura Xtreme (SLA) | 3D Systems 3dsystems.com. https://www.3dsystems.com/materials/accura-xtreme. [Accessed 31.08.2023].
- [19] A. Sciacchitano and B. Wieneke. PIV uncertainty propagation. *Measurement Science and Technology*, 27(8):084006, 2016.
- [20] F. M. Heckmeier, S. Hayböck, and C. Breitsamter. Spatial and temporal resolution of a fast-response aerodynamic pressure probe in grid-generated turbulence. *Experiments in Fluids*, 62(2), 2021.
- [21] MATHWORKS. 3-D locations of undistorted matching points in stereo images MATLAB triangulate MathWorks Deutschland de.mathworks.com. https://de.mathworks.com/help/vision/ref/triangulate.html?s_tid=srchtitle_site_search_1_triangulate. [Accessed 18-04-2024].
- [22] ANSYS. Ansys Fluent User's Guide. ANSYS, Inc.: Canonsburg, PA, USA, 2023.
- [23] C. Breitsamter. Unsteady flow phenomena associated with leading-edge vortices. *Progress in Aerospace Sciences*, 44(1):48–65, 2008.
- [24] D. Sedlacek, F. M. Heckmeier, A. Usbek, and C. Breitsamter. *Analysis of Vortex Burst Phenomena on Generic Hybrid Delta Wing Planforms at Subsonic Speeds*, page 282–291. Springer International Publishing, 2021.